frontiers | Frontiers in Microbiology

TYPE Original Research
PUBLISHED 21 January 2025
DOI 10.3389/fmicb.2025.1475572

OPEN ACCESS

EDITED BY
Carmen Falagan,
University of Portsmouth, United Kingdom

REVIEWED BY
Alfonso Mazuelos Rojas,
University of Seville, Spain
Linghao Kong,
Chinese Academy of Sciences (CAS), China

*CORRESPONDENCE
Jin-lan Xia
✉ jlxia@csu.edu.cn
Hong-chang Liu
✉ hchliu2050@csu.edu.cn

RECEIVED 04 August 2024
ACCEPTED 07 January 2025
PUBLISHED 21 January 2025

CITATION
Zheng X-f, Xia J-l, Nie Z-y, Cao H-p, Hu R-J, Liang Y-t and Liu H-c (2025) The promotion effect of FeS_2 on Sb_2S_3 bioleaching and Sb speciation transformation.
Front. Microbiol. 16:1475572.
doi: 10.3389/fmicb.2025.1475572

The promotion effect of FeS_2 on Sb_2S_3 bioleaching and Sb speciation transformation

Xing-fu Zheng[1,2,3], Jin-lan Xia[1,3]*, Zhen-yuan Nie[1,3], Hong-peng Cao[1,3], Rui-Jia Hu[2], Yu-ting Liang[1] and Hong-chang Liu[1,3]*

[1]School of Minerals Processing and Bioengineering, Central South University, Changsha, China, [2]Guangxi Academy of Sciences, Nanning, China, [3]Key Lab of Biometallurgy of Ministry of Education of China, Central South University, Changsha, China

Stibnite (Sb_2S_3) is an important but difficult to biologically leach mineral, so it is important to find a potential scheme for improving the bioleaching rate of Sb_2S_3. In this study, by combining experiments and first-principles density functional theory (DFT) calculations, the impact and related mechanisms of pyrite (FeS_2) on stibnite (Sb_2S_3) bioleaching were studied for the first time. The bioleaching results revealed that FeS_2 obviously improved the Sb_2S_3 bioleaching rate, and in the $0.5FeS_2$:$0.5CuFeS_2$ system, the bioleaching rate of Sb_2S_3 increased from 2.23 to 24.6%, which was the best mass mixing ratio. The XPS and XANES results revealed that during the bioleaching process, Sb_2S_3 was transformed to Sb_2O_3 and Sb_2O_5. The electrochemical results revealed that after FeS_2 was mixed, a FeS_2-Sb_2S_3 galvanic cell formed, which promoted the electron transfer efficiency and redox reaction of Sb_2S_3. The DFT results show that between the Sb_2S_3 (0 1 0) and FeS_2 (1 0 0) surfaces, S-Fe, S-S, S-Sb, and Sb-Fe bonds are formed, and the direction of electron transfer is from Sb_2S_3 to FeS_2; the work functions for Sb_2S_3 after addition of FeS_2 decrease, implying that faster electron transfer occurs; Fe(III)-$6H_2O$ derived from FeS_2 adsorbs on the surface more easily than does glucose, which is the major component of the extracellular polymeric substances in bacteria, indicating that during the bioleaching process, Fe(III)-$6H_2O$ plays an important role; after mixing, both Fe(III)-$6H_2O$ and glucose adsorb on the Sb_2S_3 (0 1 0) surface more easily, with stronger bonds and larger adsorption energies, which are in good agreement with the experimental results.

KEYWORDS

Sb_2S_3, FeS_2, bioleaching, XANES spectroscopy, electrochemistry, DFT calculations

1 Introduction

Antimony (Sb) plays an important role in social development and is used in storage batteries, printing industries, semiconductors, and pharmaceuticals (Awe and Sandström, 2013; Zhang et al., 2019) and is an important strategic material. Currently, via the pyrometallurgical route, Sb can be extracted from stibnite (Sb_2S_3), which is the most important and ubiquitous antimony ore (Biver and Shotyk, 2012; Multani et al., 2016), but such a method results in high-energy consumption and environmental pollution. In addition, with the mining of antimony ore and the decrease in high-grade antimony ores, there is a need to develop new methods to extract Sb from low-grade ores or tailings.

Bioleaching is a green, low-cost, and low-emission technology used to extract metal ions from ores (Hong et al., 2023; Zhao et al., 2020), and plenty of bioleaching research has been carried out on sulfide ore. For Sb_2S_3, several researchers have explored the dissolution process

of Sb_2S_3 and reported that microorganisms play important roles in the release, migration, and transformation processes of Sb_2S_3 (Bagherifam et al., 2021; Loni et al., 2020), as well as the environmental processes and relevant molecular mechanisms of antimony in mining areas (Wang et al., 2020; Yang and He, 2015; Ye et al., 2020). These studies have focused mainly on the environmental effects of environmental microorganisms. The use of acidophiles to extract Au from refractory gold ores containing abundant stibnite and gudmundite has also been studied (de Carvalho et al., 2019); recently, we studied the dissolution of stibnite mediated by *Acidithiobacillus ferrooxidans* (*A. ferrooxidans*) and relevant Sb and S speciation transformations and reported that *A. ferrooxidans* can enhance the leaching process of stibnite in comparison with sterile control experiments (Wang et al., 2022). During the bioleaching process, microorganisms convert antimony through direct oxidation or indirect reduction, that is, Sb(III) is oxidized as an energy metabolism substrate to Sb(V), as shown in Equations (1)–(3), obtaining the energy required for its growth (Loni et al., 2020; Lu et al., 2018). However, the bioleaching rate is not high because of the toxicity and insolubility of Sb_2S_3. Therefore, it is necessary to study methods to improve the antimony leaching rate. The associated minerals significantly impact on mineral dissolution (Multani et al., 2016; Wilson et al., 2004); however, few studies have investigated about how pyrite (FeS_2), a common natural mineral associated with Sb_2S_3, affects the bioleaching rate of Sb_2S_3 (Yan et al., 2020) and the transformation process of Sb during the bioleaching process, and the related mechanisms are still unclear.

$$Sb_2S_3(s) \xrightarrow{Microbial} Sb^{3+}(aq) + S^{2-}(aq) \quad (1)$$

$$Sb^{3+}(aq) \xrightarrow{Microbial} Sb^{5+}(aq) + 2e^- \quad (2)$$

$$Sb^{5+}(aq) + 5H_2O(l) \xrightarrow{Microbial} Sb_2O_5(s) + 10H^+(aq) + 5e^- \quad (3)$$

In the present study, the effects of FeS_2 on the fate and speciation transformation of Sb during the bioleaching of stibnite were studied via synchrotron radiation-based Sb X-ray near-edge structure (XANES) spectroscopy, and X-ray photoelectron spectroscopy (XPS) analyses, combined with density functional theory (DFT) calculations. In bioleaching bacterial strains, e.g., *Sulfobacillus thermosulfidooxidans* (Liu et al., 2024; Li, 2017), extracellular polymeric substances (EPS) are important components that are beneficial for bacterial adhesion processes (Wang et al., 2010), and glucose is the major sugar component in EPS (Gehrke et al., 1998); thus, in DFT calculations, glucose is utilized to simulate the interactions between bacteria and minerals (Zheng et al., 2020), and the Fe(III)-$6H_2O$ that is oxidized from FeS_2 is also considered to simulate indirect effects during the bioleaching process (Zheng et al., 2019; Magini, 1979; Magini and Radnai, 1979). This study aims to understand the element migration mechanism in the Sb mining area, thus further identifying a potential scheme for improving the bioleaching rate of Sb_2S_3. To our knowledge, reports exploring the interfacial interactions for the FeS_2-Sb_2S_3 bioleaching system by combining experiments and DFT calculations are rare.

2 Materials and methods

2.1 Minerals

The minerals Sb_2S_3 and FeS_2 were provided by the School of Minerals Processing and Bioengineering, Central South University, Changsha, China. The XRD (X-ray diffraction patterns) results in Figure 1 revealed that the pyrite is pure, and the stibnite is mainly composed of Sb_2S_3 and quartz. Furthermore, the composition of stibnite was determined by XRF (X-ray fluorescence), and the results (Supplementary Table S1) show that Sb, S, and Si are the main components, with a small amount of Al. The ICP (inductively coupled plasma-optical emission spectroscopy) results revealed that the contents of Sb, S, and Fe were 2:3:0. Before the bioleaching tests, the mineral samples were crushed and milled to 37–74 μm particle sizes.

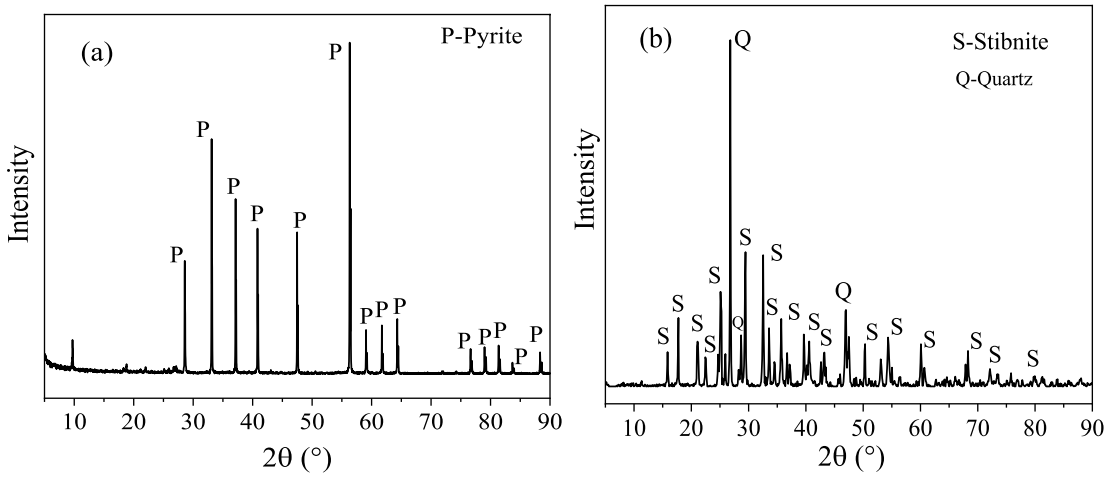

FIGURE 1
XRD results for FeS_2 **(A)** and Sb_2S_3 **(B)**.

FeS_2 and Sb_2S_3 were mixed well at weight ratios of 0:1, 0.1:0.9, 0.2:0.8, 0.3:0.7, 0.5:0.5, and 0.8:0.2.

2.2 Bioleaching experiments

For the bioleaching experiments, the mixed samples were used as energy substrates, and the pulp density was 1% (w/v). The bacterium, *Sulfobacillus thermosulfidooxidans* YN22 (*S. thermosulfidooxidans*), provided by the School of Minerals Processing and Bioengineering, was used; the inoculation concentration was 4×10^7 cells/mL in 100 mL 9 K medium, and the pH was adjusted to 2.0. Then, the flasks were placed in a rotary shaker at 180 rpm and 45°C. The pH and ORP during the bioleaching process were determined by a pH meter (PHS-3C) and Pt electrode using a calomel electrode (Ag/AgCl) as the reference, respectively; the concentrations of Sb and Fe were determined by ICP (SPECTROBLUE FMX26, Philadelphia, PA, United States), and the concentration of [Fe^{3+}] was determined by the sulfosalicylic acid method. In detail, for [Sb] and [TFe], 1 mL of solution was collected, diluted with 10% nitric acid, and preserved at −80°C until analysis; for [Fe^{3+}], 1 mL of solution was collected in the anaerobic chamber and diluted with prepared anaerobic water; then, 300 μL of 10% sulfosalicylic acid solution and 300 μL of diluted solution were added into a colorimetric tube, quantified to 10 mL with distilled water, shaken well, and then the mixed solution was measured using a microplate spectrophotometer at a wavelength of 500 nm. All the experiments were conducted in triplicate.

2.3 Residues composition analysis

The solid leaching residues were collected after leaching for 0, 5, and 10 days, washed three times with diluted sulfuric acid (pH 2.0) and hydrochloric acid (pH 2.0), and stored at −70°C. The surface morphologies of the residues were determined by scanning electron microscopy (SEM, Nano230, FEI) coupled with energy dispersive spectroscopy (EDS). In detail, the samples were prefixed with 25% formaldehyde, dehydrated via a graded ethanol series, coated with gold nanoparticles, and introduced into the SEM chamber for observation.

The residues phase compositions were analyzed by XRD in the range of 10–90° on a Bruker D8 instrument (BrukerAXS) with Cu Kα radiation The Sb speciation of the solid residue was analyzed by X-ray photoelectron spectroscopy (XPS). Briefly, XPS spectra were collected by an X-ray photoelectron spectrometer (Thermo Scientific K-Alpha+, United Kingdom) with a voltage and current of 12 kV and 6 mA, respectively. The obtained XPS data were analyzed in CasaXPS software, and all photoelectron binding energies were referenced to the C1s adventitious contamination peak set at 284.5 eV BE. Furthermore, Sb L-edge XANES spectroscopy was performed at beamline 4B7A in the Beijing Synchrotron Radiation Facility, Beijing, China. The Sb L-edge XANES spectra were recorded in total electron yield (TEY) mode with a step size of 0.1 eV and a dwell time of 2 s at each energy at 25°C from 4.60 to 4.80 keV across the Sb L-edge. Owing to the easy oxidization of the sample surfaces, all samples and tests were performed under strict anaerobic conditions with high-purity nitrogen gas (Goh et al., 2006), and were detected under the same conditions and parameter settings. The XANES spectra were normalized to the maximum of the absorption spectrum using reference spectra with the IFEFFIT program (Ide-Ektessabi et al., 2004; Prange, 2008; Ravel and Newville, 2005).

2.4 Electrochemical experiments

Electrochemical measurements were performed in 9 K medium (pH 2.0) via an electrochemical working station (INTERFACE 1010E, GAMRY, America). A conventional three-electrode system was used, including a counter electrode (carbon rods), a reference electrode (Ag/AgCl), and a working electrode (mineral electrode). The working electrodes were prepared by mixing 0.3 g graphite, 1.05 g minerals, and 0.15 g solid paraffin, and then the mixture was compressed at 120 KPa for 10 min. The Tafel curves were tested from −200 to +750 mV (vs open circuit potential, OCP) with a scan rate of 1 mV/s; the EIS (electrochemical impedance spectroscopy) curves were tested in the frequency range of 10^{-1} to 10^{-5} Hz, and fitted by Gamry Echem Analyst; the forward CV (cyclic voltammetry) was scanned from −1.0 to +1.0 V, while the reversed CV from +1.0 to −1.0 V. To explore the role of bacteria, *S. thermosulfidooxidans* was added to the medium with an inoculation amount of $2*10^8$ cells/mL during the CV test. In this study, all the potentials reported were expressed vs. Ag/AgCl.

2.5 Computational details

The DFT calculations were performed via CASTEP (Cambridge Sequential Total Energy Package) (Segall et al., 2002) and GGA-PBE (Generalized gradient approximation-Perdew-Burke-Ernzerhof functional) (Perdew et al., 1996; Segall et al., 2002), in which only the valence electrons were considered explicitly using ultrashort pseudopotentials (Vanderbilt, 1990). Sb_2S_3 belongs to the space group Pmn21 (Park et al., 2010), and FeS_2 belongs to the space group Th^6-Pa3 (Qiu et al., 2004). After obtaining the Sb_2S_3 (0 1 0) surface and the FeS_2 (1 0 0) surface, which are the most stable surfaces of the two sulfide ores (Blanchard et al., 2007; Cao et al., 2018; de Lima et al., 2011; de Oliveira et al., 2012), the supercells were built with a vacuum slab of 15 Å to avoid adjacent interlayer interactions (Fan et al., 2017). The FeS_2-Sb_2S_3 interaction model was built by using building layer tools, and the calculation was performed after constraining the model size. A $3 \times 3 \times 1$ k-point and 500 eV cutoff energy were used for the calculations. Glucose and Fe(III)-$6H_2O$ were optimized in a $15 \times 15 \times 15$ Å slab. The convergence tolerances were set to a maximum displacement of 0.002 Å, a maximum force of 0.05 eV/Å, a maximum energy change of 2.0×10^{-5} eV/atom, and a maximum stress of 0.1 GPa, while the SCF convergence tolerance was set to 2.0×10^{-6} eV/atom. For all the calculations, spin polarization, dipole correction, and DFT-D correction were considered. The frontier orbitals, HOMO-LUMO, were calculated in $DMol^3$. According to previous work, the calculation method above can provide reliable results for Sb_2S_3 and FeS_2 (Cao et al., 2018; Cao et al., 2020; Zheng et al., 2018).

The glucose or Fe(III)-$6H_2O$ adsorption energies (E_{ads}) can be calculated using equation 4:

$$E_{ads} = E_{(FeS2-Sb2S3-adsorbate)} - \left(E_{FeS2-Sb2S3} + E_{adsorbate}\right) \quad (4)$$

where $E_{FeS2\text{-}CuFeS2}$, $E_{adsorbate}$, and $E_{(FeS2\text{-}CuFeS2\ -\ adsorbate)}$ represent the total energies for the clean FeS_2-Sb_2S_3 surface, the free glucose/Fe(III)-$6H_2O$, and the FeS_2-Sb_2S_3–adsorbate system, respectively.

3 Results and discussion

3.1 Leaching parameters

The results (Figure 2) show that by adding FeS_2, the pH decreases faster while the ORP increases faster, implying that the dissolution process of Sb_2S_3 may be accelerated. After leaching for 5 days, the extraction rates of Sb were approximately 2.22% (Sb_2S_3), 3.15% (0.1 FeS_2: 0.9 Sb_2S_3), 4.1% (0.2 FeS_2: 0.8 Sb_2S_3), 5.7% (0.3 FeS_2: 0.7 Sb_2S_3), 24.6% (0.5 FeS_2: 0.5 Sb_2S_3), and 18.7% (0.8 FeS_2: 0.2 Sb_2S_3), where in the sterile control results (Supplementary Figure S1), the extraction rates of Sb were lower than 0.7%. After 10 days of leaching, the extraction rates of Sb decreased, and the reason may be the formation of secondary products that were found by the further results. In the 0.5 FeS_2: 0.5 Sb_2S_3 system, the Sb dissolution rate was almost 11 times higher than that of pure Sb_2S_3, indicating that such a mixing ratio is the best leaching group. In addition, Figure 2D shows that Fe^{3+} occurs after the addition of FeS_2 because FeS_2 is oxidized by *S. thermosulfidooxidans*. In addition, Fe^{3+} attacks minerals (Jiang et al., 2019), which is called indirect action, thereby accelerating the dissolution of minerals. Notably, the concentration of Fe^{3+} is lower than that of the total Fe (Supplementary Figure S2A), which is probably because of formation of Fe^{2+} (Ubaldini et al., 2000; Zhang et al., 2019), as shown in Supplementary Figure S2B. In the next section, the 0.5 FeS_2: 0.5 Sb_2S_3 mixture is analyzed further.

The XRD results (Figure 3) revealed that after 5 and 10 days of bioleaching, the peaks of FeS_2 at 47.5° weakened, implying the dissolution of FeS_2; the peak at 27° associated with Sb_2O_3 became stronger, and the peaks at 15.7° and 17.6° associated with Sb_2S_3 became weaker, indicating that Sb_2S_3 was transformed to Sb_2O_3 during bioleaching (Wang et al., 2022). Notably, in the sterile control sample, the peaks presented little or no change after 10 days of leaching. The SEM results (Figure 4; Supplementary Figure S3) show that by adding FeS_2, the Sb_2S_3 surface obviously changed after 5 days of leaching with obvious secondary products, whereas the changes in pure Sb_2S_3 (Supplementary Figure S4) were negligible, confirming the promoting

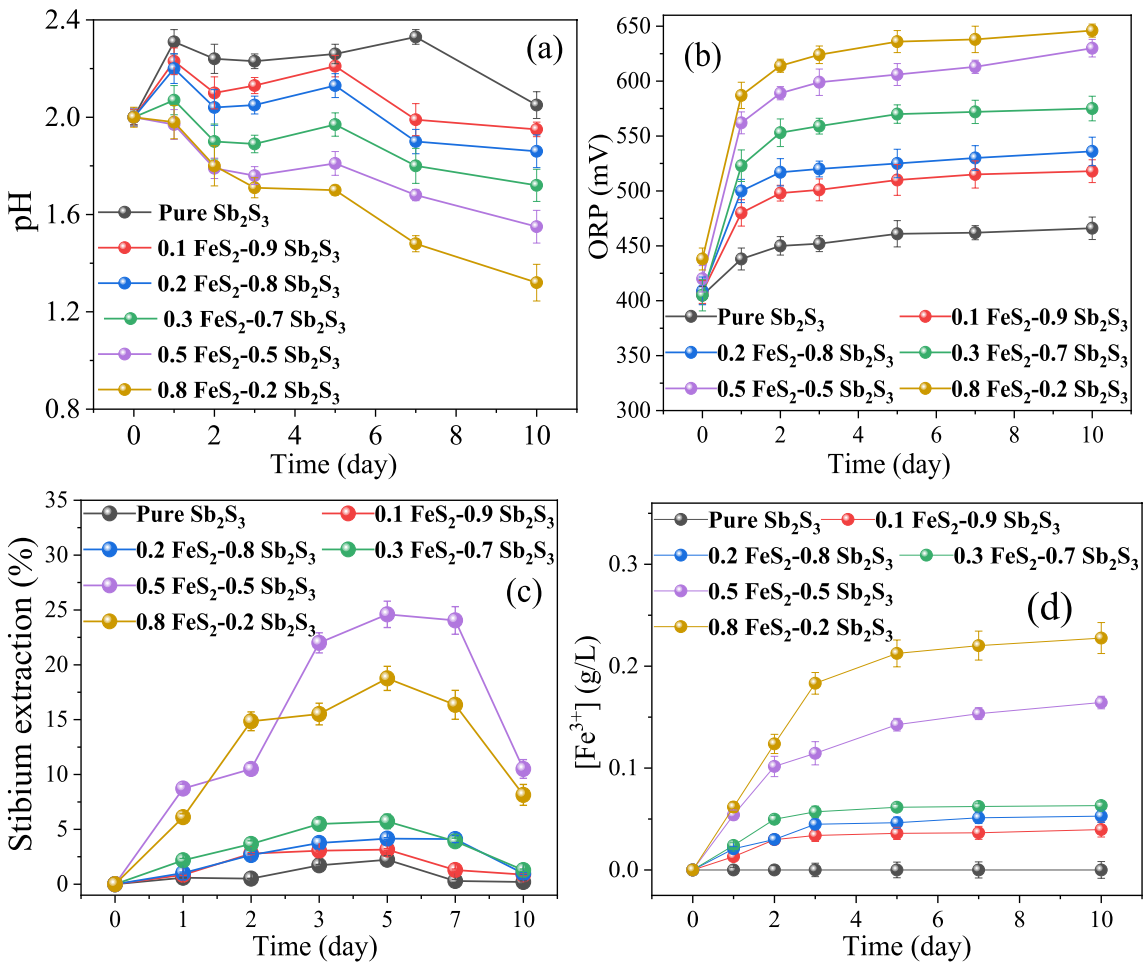

FIGURE 2
Curves for the pH **(A)**, ORP **(B)**, Sb extraction rate **(C)**, and Fe^{3+} concentration for the bioleaching of Sb_2S_3 in the presence of varying concentrations of FeS_2.

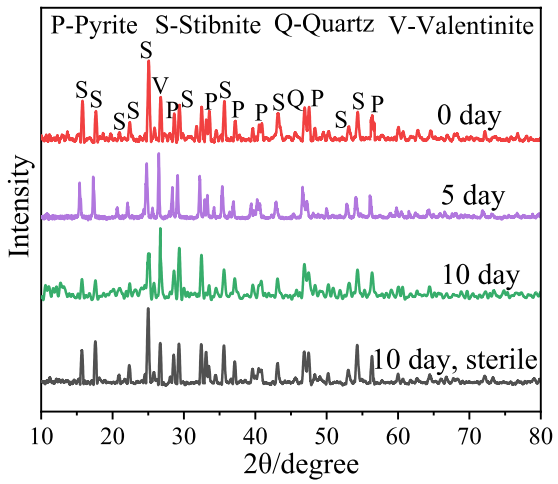

FIGURE 3
XRD of the bioleaching residues.

effect of FeS_2, and the source of secondary minerals was the dissolution of some FeS_2 (Yang et al., 2016). In addition, in the sterile control sample (Figures 4D,E), the mineral surface changed little, indicating that bacteria play an important role in the oxidation of minerals.

The XPS results (Figure 5) show that after 5 days of bioleaching, part of Sb_2S_3 (529.5 eV) (Morgan et al., 1973) was transformed to Sb_2O_3 (530.5 eV, 48.7%) and Sb_2O_5 (532.1 eV, 9%), and the proportion of Sb_2S_3 decreased from 74.6 to 42.3%; as the leaching time increased to 10 days, the proportion of Sb_2O_3 increased to 66%, and that of Sb_2O_5 increased to 9.4%, whereas the proportion of Sb_2S_3 decreased to 24.5%; in the sterile controlled experiment (Figure 5D), the proportion of Sb_2S_3 decreased to 62.4% after 10 days of leaching, which was much slower.

The Sb L-edge XANES spectra (Figure 6) show that after 5 and 10 days of bioleaching, the peak shifts from 4.7062 to 4.707 keV, indicating the conversion of Sb_2S_3 to Sb_2O_3, and the peak at 4.711 keV increases with increasing bioleaching time, which indicates the conversion of Sb(III) to Sb(V), similar to the XPS results. In addition, in the sterile controlled experiment, after 10 days, no or little Sb(III) was converted to Sb(V), confirming the important role of bacteria.

3.2 Electrochemical analyses

For mineral-mineral interactions, a galvanic effect may occur when two minerals have different corrosion potentials; however, minerals with higher potentials can act as cathodes and the other minerals with lower potential can act as anodes electrode (Ekmekqi and Demirel, 1997). The lower the value of the corrosion potential is, the easier it is for the mineral to corrode. Tafel tests were performed to analyze the mineral corrosion kinetics. The Tafel results (Figure 7A) show that the corrosion potentials (vs. Ag/AgCl) for FeS_2 and Sb_2S_3 are 428 mV and 327 mV, respectively; thus in a FeS_2-Sb_2S_3 system, the galvanic effect occurs, and Sb_2S_3 is the anode electrode, implying that the leaching rate of Sb_2S_3 is promoted (Zheng et al., 2021).

Among electrochemical methods, CV is widely used due to its simple operation and effective results for the interpretation of electrochemical reactions. The results in Figure 7 show that the oxidation peaks of Sb_2S_3 and the corresponding reduction peaks are not symmetrical, indicating that the redox reaction on the Sb_2S_3 surface is an irreversible process (Córdoba et al., 2009). Figures 7B,C shows that the CV peaks of FeS_2-Sb_2S_3 are similar to those of Sb_2S_3 (A1, B1, and C1), implying that Sb_2S_3 reacts preferentially during the electrochemical process. The current density is greater after addition of FeS_2, indicating an increase in the Sb_2S_3 reaction.

To investigate the effects of bacteria on the dissolution of Sb_2S_3, the effects of CV with *S. thermosulfidooxidans* were analyzed. Supplementary Figure S5 shows that after adding bacteria ($2*10^8$ cells/ml), the current density increased further, confirming that the bacteria can obviously enhance the leaching rate of Sb_2S_3. During the bioleaching process, some of the FeS_2 is oxidized by bacteria to produce Fe^{3+} (Yang et al., 2016), so the effect of Fe^{3+} was also studied, and the results (Supplementary Figure S6) revealed that after adding Fe^{3+} (0.15 g/L), the current density also increased, indicating that Fe^{3+} can also enhance the leaching rate of Sb_2S_3.

The electron transfer efficiency of minerals was analyzed via EIS. The data obtained were analyzed by fitting the impedance data to an appropriate equivalent circuit as Rs(Q1(R1Q2)) (Bevilaqua et al., 2009; Supplementary Figure S7). In the equivalent circuit, Rs, R1, and Q1 represent the solution resistance, ion exchange impedance, and constant phase element, respectively. Q1 is connected to the electrode interface. Q2 represents a Warburg element, and is related to the electrode/electrolyte interface diffusion process (Zeng et al., 2020). Figure 8 shows that after adding FeS_2, the curve radius decreases; the results in Table 1 show that R1 for FeS_2-Sb_2S_3 (30.71 $\Omega \cdot cm^{-2}$) is much smaller than that for Sb_2S_3 (24,300 $\Omega \cdot cm^{-2}$). Both results indicate that after mixing, the ion exchange resistance on the mineral surface decreases; in other words, after Sb_2S_3 mixed with FeS_2, the leaching system has a relatively high electron transfer efficiency, which significantly promotes the bioleaching rate.

3.3 Computational results

3.3.1 Electronic structure

The models of Sb_2S_3 and FeS_2-Sb_2S_3 are shown in Figure 9, and the corresponding atomic numbers used are shown in Supplementary Figure S8. The results in Figure 9 show that after adding FeS_2, the surface structure of Sb_2S_3 gradually became disordered, which was conducive to the dissolution of Sb_2S_3. Table 2 shows that after adding FeS_2, the Hirshfeld charge value of FeS_2 decreases from 0 to −0.77, whereas the charge value of Sb_2S_3 increases from 0 to 0.77, indicating that the direction of electron transfer is from Sb_2S_3 to FeS_2.

The bond lengths between FeS_2 and Sb_2S_3 are shown in Table 3. In the FeS_2-Sb_2S_3 galvanic cell, S-Fe, S-S, Sb-Fe, and S-Sb bonds formed at the interface, and the number of S-Fe bonds was greater than that of the other materials. S3-S23 is the shortest bond (2.128 Å), whereas Sb12-S48 is the longest bond (2.619 Å). The Mulliken bond population results show that the S2-Fe2 bond has stronger covalent interactions, and that the Sb5-S32 bond has stronger ionic interactions.

The PDOS of the S3-S23, S6-Fe5, Sb4-Fe8, and Sb6-S32 bonds were analyzed further. Figure 10 shows that in the S3-S23 bond, from −20 eV to 10 eV, the main peaks belong to σ(2 s), σ^*(2 s), σ(2p), π(2p), π^*(2p), and σ^*(2p) bonds, and the maximum overlap area between S 3p ranges from −10 eV to 5 eV, implying that σ(2p) and π(2p) are the

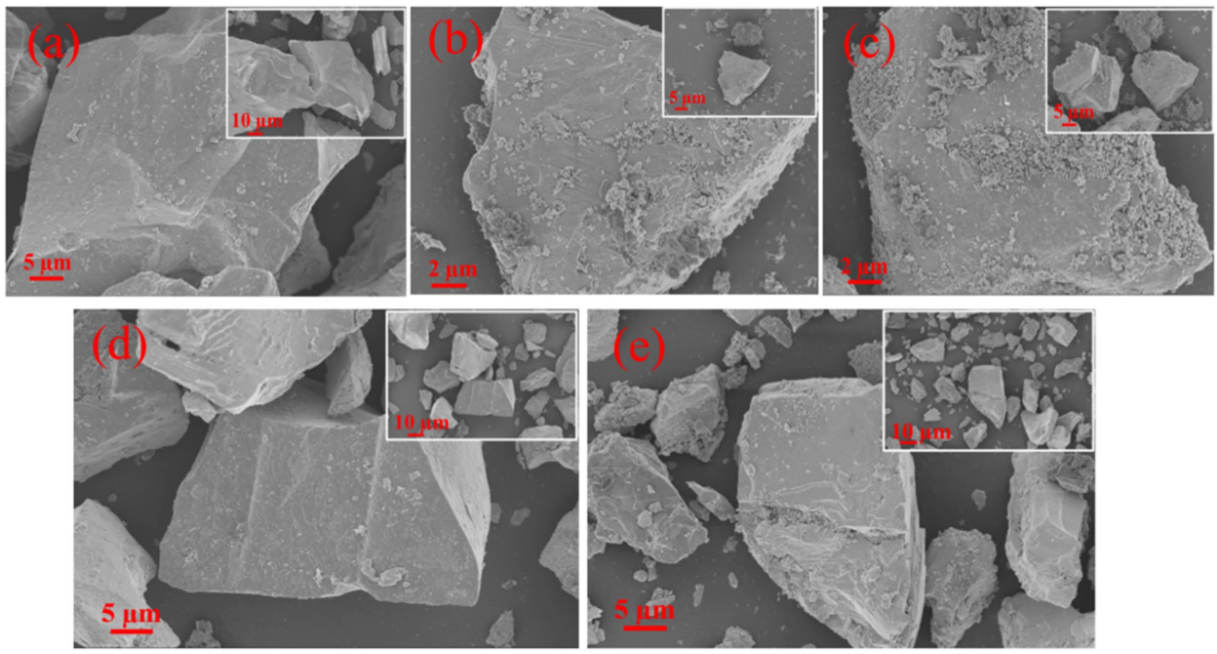

FIGURE 4
(A–C) SEM images of the bioleaching residues after 0, 5, and 10 days with the addition of FeS_2; **(D,E)** SEM images of the residues after 0 and 10 days in the sterile control.

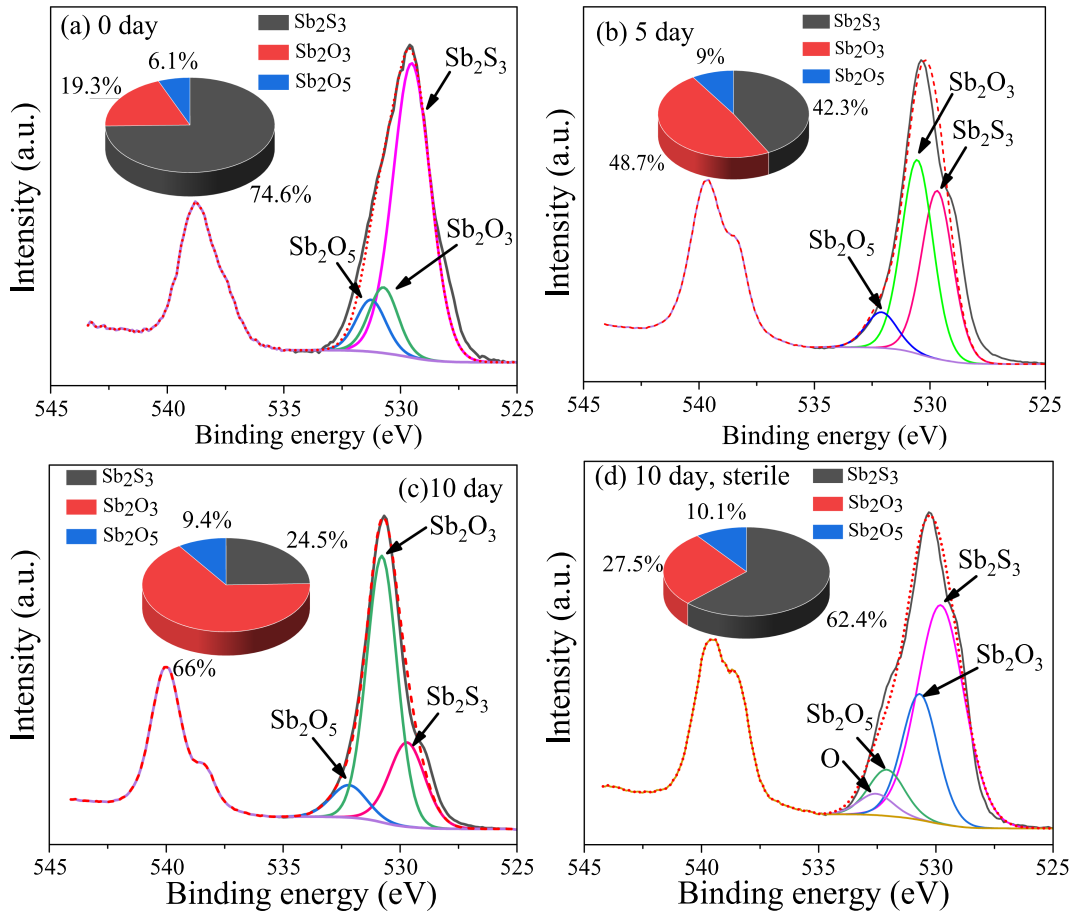

FIGURE 5
XPS spectra of Sb on the surface of the bioleaching residues.

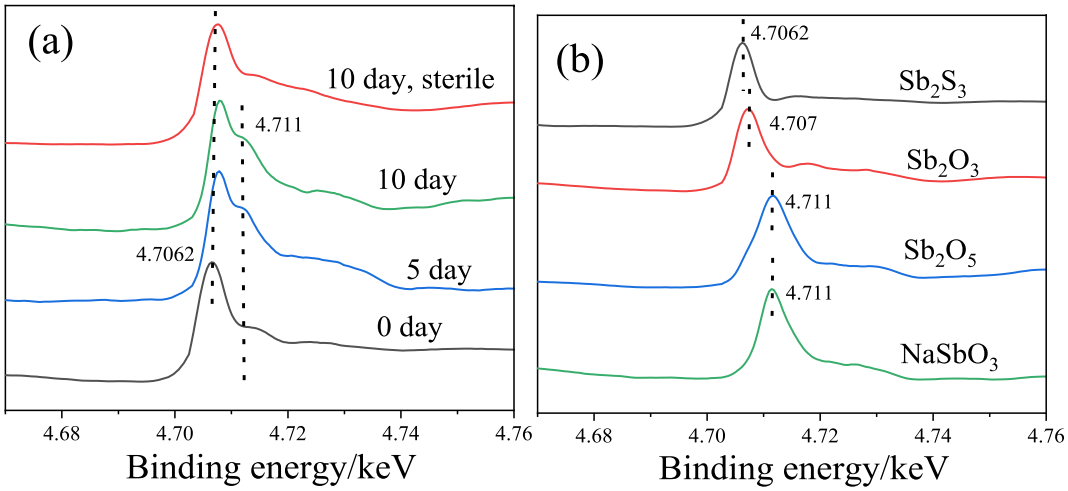

FIGURE 6
Sb L-edge XANES spectra of the residues during bioleaching **(A)** and the reference materials **(B)**.

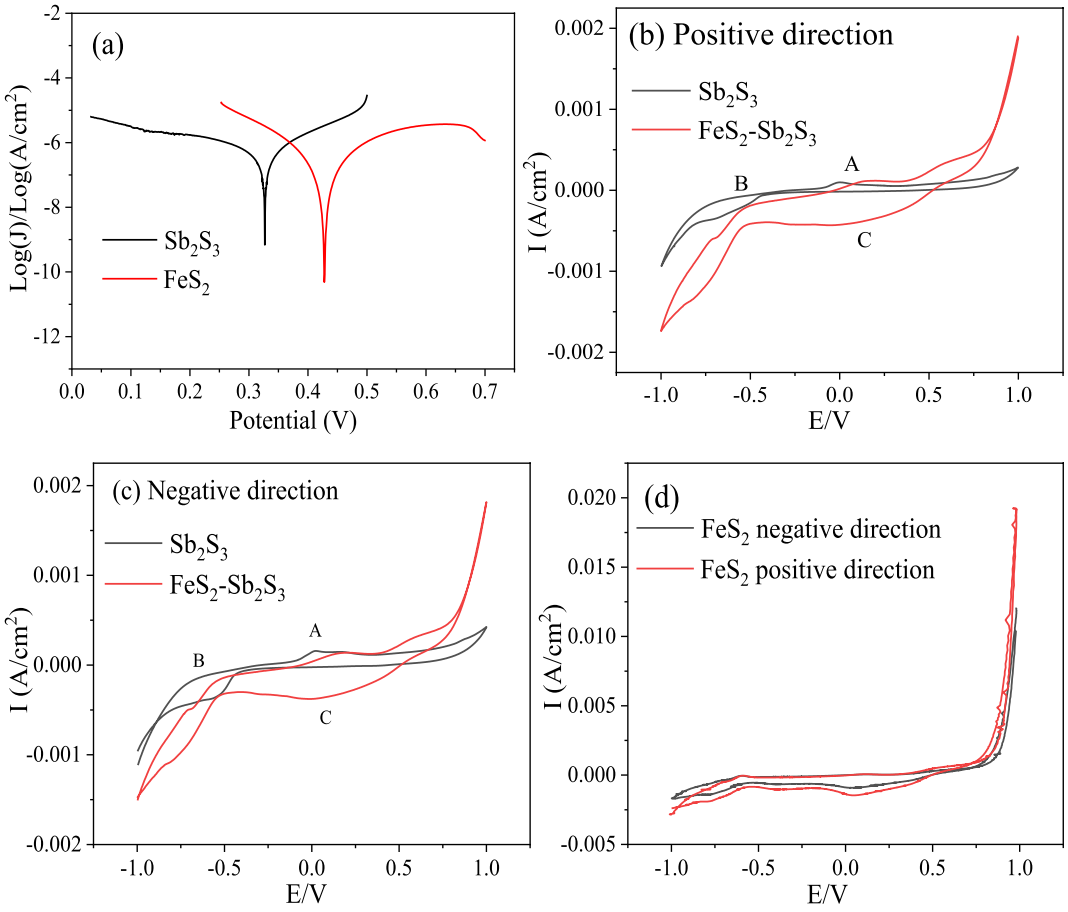

FIGURE 7
Tafel and CV curves for FeS_2, Sb_2S_3 and FeS_2-Sb_2S_3.

main covalent interactions; in the S6-Fe5 bond, from −15 eV to 5 eV, the main peaks belong to σ(s-d), σ*(s-d), π(p-d), and π*(p-d) bonds, and the maximum overlap area between S 3p and Fe 3d ranges from −10 eV to 5 eV, implying that π(p-d) are the main covalent interactions, and the same result can also be obtained in the Sb4-Fe8 bond; in the Sb6-S32 bond, the antibonding function from 0 eV to 15 eV is strong, implying weak covalent interactions, similar to the population results.

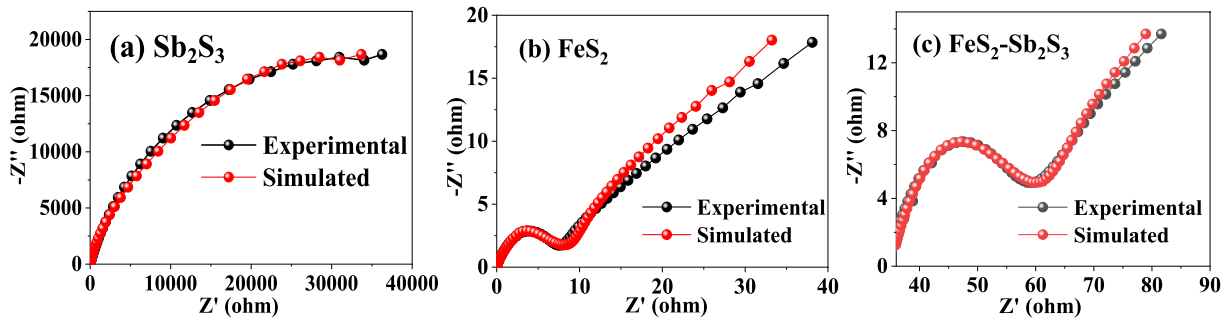

FIGURE 8
Nyquist plots for Sb_2S_3 **(A)**, FeS_2 **(B)**, and FeS_2-Sb_2S_3 **(C)**.

TABLE 1 Fitting results obtained via the circuit Rs(Q1(R1Q2)) for Sb_2S_3, FeS_2, and FeS_2-Sb_2S_3.

	Rs $\Omega \cdot cm^{-2}$	R1 $\Omega \cdot cm^{-2}$	Q1-T $S \cdot s^{a} \cdot cm^{-2}$	Q1-P $S \cdot s^{a} \cdot cm^{-2}$	Q2 $S \cdot s^{1/2} \cdot cm^{-2}$
Sb_2S_3	16.73	24,300	$1.781*10^{-5}$	0.817	$6.820*10^{-5}$
FeS_2	16.73	10	$9.25*10^{-4}$	0.753	$9.027*10^{-2}$
FeS_2-Sb_2S_3	16.73	30.71	$8.59*10^{-4}$	0.631	$7.872*10^{-2}$

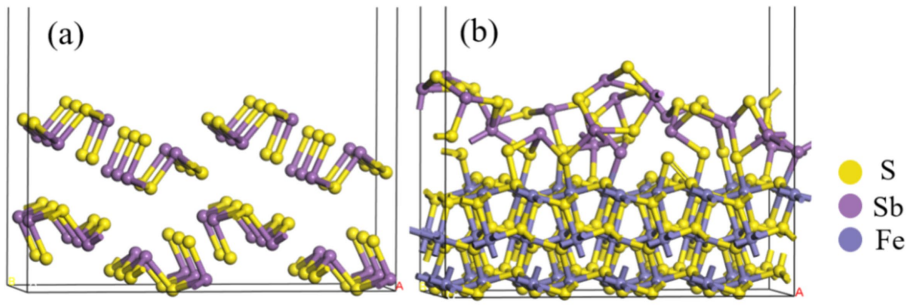

FIGURE 9
Optimized configurations of Sb_2S_3 **(A)**, and FeS_2-Sb_2S_3 **(B)**.

TABLE 2 Hirshfeld charge analysis of FeS_2-Sb_2S_3.

	Charge/e Before optimization	Charge/e After optimization
FeS_2	0	−0.77
Sb_2S_3	0	0.77

TABLE 3 Mulliken bond population analysis of FeS_2-Sb_2S_3.

Bond	Bond Lengths (Å)	Populations
S2-Fe2	2.354	0.44
S3-S23	2.128	0.25
S4-Fe4	2.307	0.44
S6-Fe5	2.267	0.42
S7-Fe6	2.491	0.32
Sb4-Fe8	2.546	0.14
Sb5-S32	2.606	0.10
S12-Fe11	2.306	0.26
S13-Fe12	2.334	0.41
S15-Fe13	2.323	0.42
S16-Fe14	2.306	0.26
Sb11-Fe16	2.547	0.21
Sb12-S48	2.619	0.20

The work functions (Figure 11) for Sb_2S_3 and FeS_2-Sb_2S_3 were calculated to be 5.17 eV, and 4.59 eV, respectively, implying that the electron transfer efficiency becomes faster after mixing, which agrees with the EIS results above.

3.3.2 Adsorption configurations and energies

In the theory of frontier orbitals, HOMO (highest occupied molecular orbital) can donate electrons, and LUMO (lowest unoccupied molecular orbital) can accept electrons (Sauer and Sustmann, 1980). According to previous studies (Sauer and Sustmann, 1980; Zheng et al., 2018), a smaller HOMO-LUMO energy difference absolute value implies a more beneficial interaction. The results in Table 4 shows that

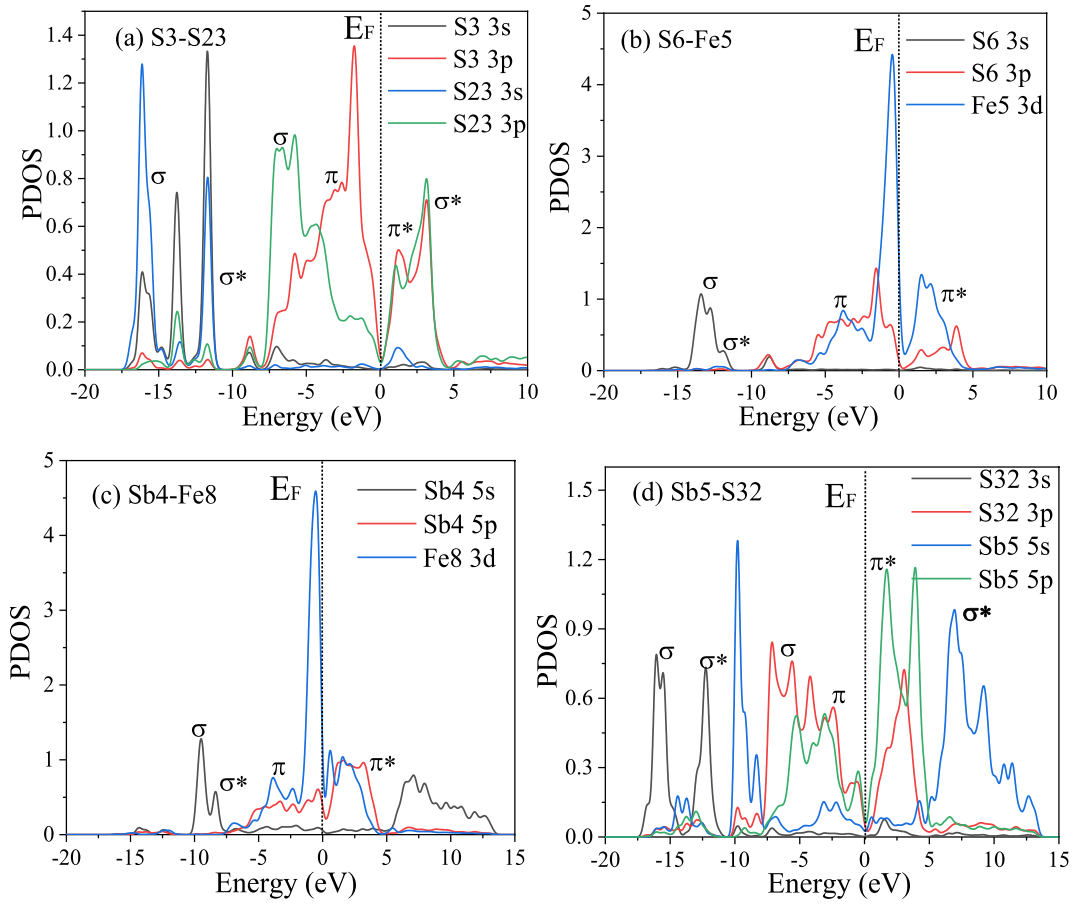

FIGURE 10
PDOS of the bonds between the FeS_2 and Sb_2S_3 surfaces.

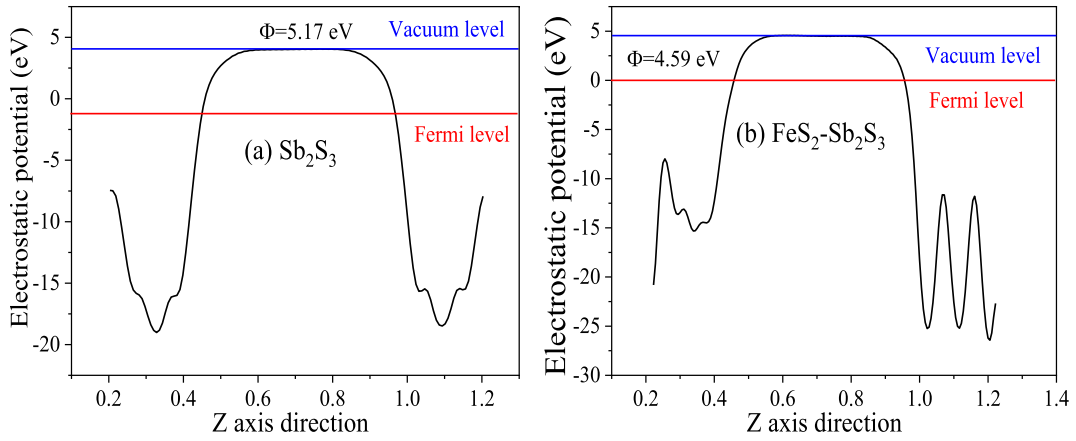

FIGURE 11
Work functions of Sb_2S_3 **(A)**, and FeS_2-Sb_2S_3 **(B)**.

TABLE 4 **Frontier orbital energies of FeS_2-$CuFeS_2$ and glucose/Fe(III)-$6H_2O$.**

	HOMO	LUMO	ΔE1	ΔE2	ΔE3	ΔE4
0.1496	0.1496	0.1496	0.1496	0.1496	0.1496	0.1496
0.1496	0.1496	0.1496	0.1496	0.1496	0.1496	0.1496
0.1496	0.1496	0.1496	0.1496	0.1496	0.1496	0.1496

$\Delta E_1 = |E(HOMO_{FeS2\text{-}Sb2S3}) - E(LUMO_{glucose})|$; $\Delta E_2 = |E(HOMO_{glucose}) - E(LUMO_{FeS2\text{-}Sb2S3})|$; $\Delta E_3 = |E(HOMO_{FeS2\text{-}Sb2S3}) - E(LUMO_{Fe(III)\text{-}6H2O})|$; $\Delta E_4 = |E(HOMO_{Fe(III)\text{-}6H2O}) - E(LUMO_{FeS2\text{-}Sb2S3})|$.

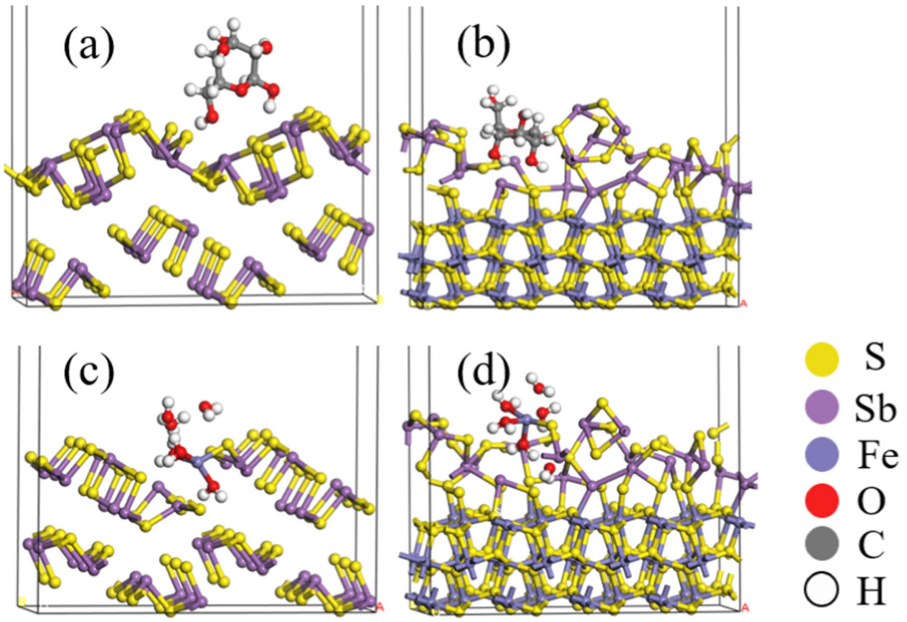

FIGURE 12
Optimized configurations of glucose **(A,B)** or Fe(III)-$6H_2O$ **(C,D)** adsorbed on Sb_2S_3, FeS_2-Sb_2S_3.

TABLE 5 Mulliken bond population analysis of FeS_2-Sb_2S_3.

	Bond (shorter one)	Bond lengths (Å)	Populations	Adsorption energies (eV)
Glucose-Sb_2S_3	O-Sb	3.093	–	0.35
Glucose-FeS_2-Sb_2S_3	O-Sb	2.907	–	0.16
Fe^{3+}-$6H_2O$- Sb_2S_3	Fe-S	2.276	0.49	−0.18
Fe^{3+}-$6H_2O$-FeS_2-Sb_2S_3	Fe-S	2.271	0.48	−0.21

TABLE 6 Hirshfeld charge analysis of Sb in Sb_2S_3.

Atom	Charge/e Before adsorption	Charge/e Glucose adsorption	Charge/e Fe^{3+}-$6H_2O$ adsorption
Sb	5.64	5.61	5.43

ΔE_2 is lower than ΔE_1, indicating that the interaction mainly occurs between the HOMO of glucose and LUMO of FeS_2-Sb_2S_3 rather than the HOMO of FeS_2-Sb_2S_3 and the LUMO of glucose; the results also show that ΔE_4 is lower than ΔE_3, implying a beneficial interaction between the HOMO of Fe(III)-$6H_2O$ and LUMO of FeS_2-Sb_2S_3.

Figures 12A,B and Table 5 show that after adding FeS_2, the bond length (Å) between glucose and the Sb_2S_3 surface becomes shorter, from 3.093 Å to 2.907 Å, and the adsorption energy decreases from 0.35 eV to 0.16 eV, indicating that FeS_2 can promote the adsorption of bacteria on the Sb_2S_3 surface, thereby enhancing bioleaching. Figures 12C,D and Table 5 show that Fe(III)-$6H_2O$ can adsorb on the Sb_2S_3 surface and has a shorter bond length and lower adsorption energy than glucose. Table 6 shows that after Fe(III)-$6H_2O$ adsorption, the charge change is more greater (−0.21) than that of glucose (−0.03). The EDD (Electron density difference) result (Figure 13) shows that there is more electron transfer between Fe(III)-$6H_2O$ and Sb_2S_3, implying stronger adsorption. Notably, the results also show that FeS_2 can promote the adsorption of Fe(III)-$6H_2O$ on the Sb_2S_3 surface, possibly because adding FeS_2 makes the Sb_2S_3 surface disordered, which is beneficial for Fe(III)-$6H_2O$ adsorption. In general, trivalent iron derived from FeS_2 has a stronger oxidation effect on Sb_2S_3 during the bioleaching process.

4 Conclusion

In this work, the effects of FeS_2 on the bioleaching of Sb_2S_3 were investigated by combining experiments and DFT calculations, and the results can be summarized as follows: (1) After adding FeS_2, the bioleaching rate of Sb_2S_3 increased significantly, from 2.23 to 24.6% after 5 days of bioleaching, and the best mass mixing ratio was 0.5:0.5; (2) During the bioleaching process, Sb_2S_3 was gradually transformed

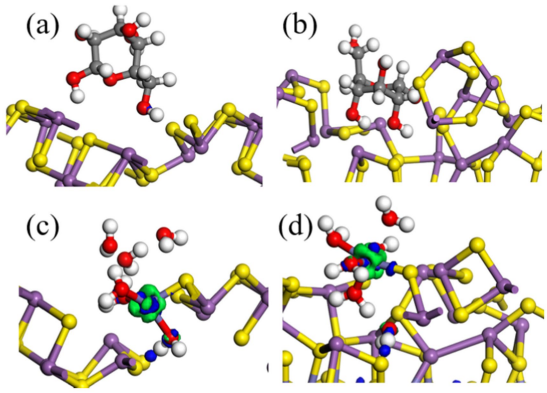

FIGURE 13
(A,B) Electron density difference for the interaction between glucose and the Sb_2S_3, FeS_2-Sb_2S_3 surface; **(C,D)** electron density difference for the interaction between Fe(III)-$6H_2O$ and the Sb_2S_3, or FeS_2-Sb_2S_3 surface. The green area represents electron loss, and the blue contours indicate an increase in the electron density.

to Sb_2O_3 and Sb_2O_5; (3) Adding FeS_2 can form a FeS_2-Sb_2S_3 galvanic cell, which has a greater redox reaction current density, and faster electronic delivery efficiency; and (4) The DFT results indicated that after mixing, both Fe(III)-$6H_2O$ and glucose could adsorb onto the Sb_2S_3 (0 1 0) surface more easily, and Fe(III)-$6H_2O$ may play a major role in Sb_2S_3 bioleaching.

Data availability statement

The original contributions presented in the study are included in the article/Supplementary material, further inquiries can be directed to the corresponding authors.

Author contributions

X-fZ: Methodology, Resources, Software, Validation, Visualization, Writing – original draft, Writing – review & editing. J-lX: Funding acquisition, Resources, Supervision, Visualization, Writing – original draft, Writing – review & editing. Z-yN: Formal analysis, Methodology, Resources, Supervision, Writing – review & editing. H-pC: Investigation, Methodology, Resources, Writing – review & editing. R-JH: Formal analysis, Supervision, Writing – review & editing. Y-tL: Data curation, Methodology, Supervision, Writing – review & editing. H-cL: Funding acquisition, Methodology, Visualization, Writing – original draft, Writing – review & editing.

Funding

The author(s) declare financial support was received for the research, authorship, and/or publication of this article. This study was funded by the National Natural Science Foundation of China (NSFC) (Nos. 41830318 and 51861135305), and the National Supercomputing Center in Shenzhen (Shenzhen Cloud Computing Center), China.

Acknowledgments

The authors of this article acknowledge the technical team at the Key Lab of Biometallurgy of Ministry of Education of China, Central South University.

Conflict of interest

The authors declare that the research was conducted in the absence of any commercial or financial relationships that could be construed as a potential conflict of interest.

Publisher's note

Supplementary material

The Supplementary material for this article can be found online at: https://www.frontiersin.org/articles/10.3389/fmicb.2025.1475572/full#supplementary-material

References

Awe, S. A., and Sandström, Å. (2013). Electrowinning of antimony from model sulphide alkaline solutions. *Hydrometallurgy* 137, 60–67. doi: 10.1016/j.hydromet.2013.04.006

Bagherifam, S., Brown, T. C., Wijayawardena, A., and Naidu, R. (2021). The influence of different antimony (Sb) compounds and ageing on bioavailability and fractionation of antimony in two dissimilar soils. *Environ. Pollut.* 270:116270. doi: 10.1016/j.envpol.2020.116270

Bevilaqua, D., Acciari, H. A., Arena, F. A., Benedetti, A. V., Fugivara, C. S., Filho, G. T., et al. (2009). Utilization of electrochemical impedance spectroscopy for monitoring bornite (Cu_5FeS_4) oxidation by *Acidithiobacillus ferrooxidans*. *Miner. Eng.* 22, 254–262. doi: 10.1016/j.mineng.2008.07.010

Biver, M., and Shotyk, W. (2012). Stibnite (Sb_2S_3) oxidative dissolution kinetics from pH 1 to 11. *Geochim. Cosmochim. Acta* 79, 127–139. doi: 10.1016/j.gca.2011.11.033

Blanchard, M., Wrigh, K., Gale, J. D., and Catlow, C. R. A. (2007). Adsorption of as$(OH)_3$ on the (0 0 1) surface of FeS_2 pyrite: a quantum-mechanical DFT study. *J. Phys. Chem. C* 111, 11390–11396. doi: 10.1021/jp072468v

Cao, Q., Chen, X., Feng, Q., and Wen, S. (2018). Activation mechanism of lead ion in the flotation of stibnite. *Miner. Eng.* 119, 173–182. doi: 10.1016/j.mineng.2018.01.039

Cao, S., Zheng, X., Nie, Z., Zhou, Y., Liu, H., Chen, J., et al. (2020). Mechanical activation on bioleaching of chalcopyrite: a new insight. *Fortschr. Mineral.* 10:788. doi: 10.3390/MIN10090788

Córdoba, E. M., Muñoz, J. A., Blázquez, M. L., González, F., and Ballester, A. (2009). Passivation of chalcopyrite during its chemical leaching with ferric ion at 68°C. *Miner. Eng.* 22, 229–235. doi: 10.1016/j.mineng.2008.07.004

de Carvalho, L. C., da Silva, S. R., Giardini, R. M. N., de Souza, L. F. C., and Leão, V. A. (2019). Bio-oxidation of refractory gold ores containing stibnite and gudmundite. *Environ. Technol. Innov.* 15:100390. doi: 10.1016/j.eti.2019.100390

de Lima, G. F., de Oliveira, C., de Abreu, H. A., and Duarte, H. A. (2011). Water adsorption on the reconstructed (001) chalcopyrite surfaces. *J. Phys. Chem. C* 115, 10709–10717. doi: 10.1021/jp201106e

de Oliveira, C., de Lima, G. F., de Abreu, H. A., and Duarte, H. A. (2012). Reconstruction of the chalcopyrite surfaces—a DFT study. *J. Phys. Chem. C* 116, 6357–6366. doi: 10.1021/jp300713z

Ekmekqi, Z., and Demirel, H. (1997). Effects of galvanic interaction on collectorless flotation behaviour of chalcopyrite and pyrite. *Int. J. Miner. Process.* 52, 31–48. doi: 10.1016/S0301-7516(97)00050-1

Fan, Y., Zhang, J., Qiu, Y., Zhu, J., Zhang, Y., and Hu, G. (2017). A DFT study of transition metal (Fe, co, Ni, cu, ag, au, Rh, Pd, Pt and Ir)-embedded monolayer MoS_2 for gas adsorption. *Comput. Mater. Sci.* 138, 255–266. doi: 10.1016/j.commatsci.2017.06.029

Gehrke, T., Telegdi, J., Thierry, D., and Sand, W. (1998). Importance of extracellular polymeric substances from *Thiobacillus ferrooxidans* for bioleaching. *Appl. Environ. Microb.* 64, 2743–2747. doi: 10.1128/AEM.64.7.2743-2747.1998

Goh, S. W., Buckley, A. N., Lamb, R. N., Rosenberg, R. A., and Moran, D. (2006). The oxidation states of copper and iron in mineral sulfides, and the oxides formed on initial exposure of chalcopyrite and bornite to air. *Geochim. Cosmochim. Acta* 70, 2210–2228. doi: 10.1016/j.gca.2006.02.007

Hong, M., Lin, M., Yang, B., Xiao, J., Liao, R., and Yu, S. (2023). Evolution of passivating species on bornite surface during electrochemical dissolution. *Trans. Nonferr. Metal. Soc.* 33, 1906–1918. doi: 10.1016/s1003-6326(23)66231-4

Ide-Ektessabi, A., Kawakami, T., and Watt, F. (2004). Distribution and chemical state analysis of iron in the parkinsonian substantia nigra using synchrotron radiation micro beams. *Nucl. Instrum. Meth. B* 213, 590–594. doi: 10.1016/S0168-583X(03)01755-5

Jiang, L., Wei, D., Liu, W., Liu, K., and Zhang, H. (2019). Effects of Fe^{3+} and ag^{+} on column bioleaching of a low-grade sulfide copper ore. *Int. J. Electrochem. Sci.* 14, 6303–6314. doi: 10.20964/2019.07.43

Li, Q. (2017). Extracellular polymeric substances involved in adhesion and biofilm formation by *Sulfobacillus thermosulfidooxidans*. Germany: Universität Duisburg-Essen Durchgeführt.

Liu, A., Yu, R., Qiu, G., and Zeng, W. (2024). Insights into the EPS production and distribution of planktonic and attached *Sulfobacillus thermosulfidooxidans* cells during bioleaching. *Miner. Eng.* 205:108494. doi: 10.1016/j.mineng.2023.108494

Loni, P., Wu, M., Wang, W., Wang, H., and Tuovonen, O. (2020). Mechanism of microbial dissolution and oxidation of antimony in stibnite under ambient conditions. *J. Hazard. Mater.* 385:121561. doi: 10.1016/j.jhazmat.2019.121561

Lu, X., Zhang, Y., Liu, C., Wu, M., and Wang, H. (2018). Characterization of the antimonite.and arsenite-oxidizing bacterium Bosea sp, AS-1 and its potential application in ar-senic removal. *J. Hazard. Mater.* 359, 527–534. doi: 10.1016/j.jhazmat.2018.07.112

Magini, M. (1979). Solute structuring in aqueous iron(III) sulphate solutions. Evidence for the formation of iron (III)-sulphate complexes. *J. Chem. Phys.* 70, 317–324. doi: 10.1063/1.437193

Magini, M., and Radnai, T. (1979). X-ray diffraction study of ferric chloride solutions and hydrated melt. Analysis of the iron(III)-chioride complexes formation. *J. Chem. Phys.* 71, 4255–4262. doi: 10.1063/1.438233

Morgan, W., Stec, W., and Wazer, J. (1973). Inner-orbital binding-energy shifts of antimony and bismuth compounds. *Inorg. Chem.* 12, 953–955. doi: 10.1021/ic50122a054

Multani, R. S., Feldmann, T., and Demopoulos, G. P. (2016). Antimony in the metallurgical industry: a review of its chemistry and environmental stabilization options. *Hydrometallurgy* 164, 141–153. doi: 10.1016/j.hydromet.2016.06.014

Park, C. M., Hwa, Y., Sung, N. E., and Sohn, H. J. (2010). Stibnite (Sb_2S_3) and its amorphous composite as dual electrodes for rechargeable lithium batteries. *J. Mater. Chem.* 20, 1097–1102. doi: 10.1039/B918220A

Perdew, J. P., Burke, K., and Ernzerhof, M. (1996). Generalized gradient approximation made simple. *Phy. Rev. Lett.* 77, 3865–3868. doi: 10.1103/PhysRevLett.77.3865

Prange, A. (2008). "Speciation analysis of microbiologically produced sulfur by X-ray absorption near edge structure spectroscopy," in *Microbial sulfur metabolism*. (Heidelberg, Berlin: Springer Berlin Heidelberg Press). 259–272.

Qiu, G., Xiao, Q., Hu, Y., Qin, W., and Wang, D. (2004). Theoretical study of the surface energy and electronic structure of pyrite FeS_2 (100) using a total-energy pseudopotential method, CASTEP. *J. Colloid Interf. Sci.* 270, 127–132. doi: 10.1016/j.jcis.2003.08.028

Ravel, B., and Newville, M. (2005). HEPHAESTUS: data analysis for X-ray absorption spectroscopy using IFEFFIT. *Synchrotron. Radiat.* 12, 537–541. doi: 10.1107/s0909049505012719

Sauer, J., and Sustmann, R. (1980). Mechanistic aspects of Diels-Alder reactions a critical survey. *Angew. Chem. Inr. Ed. Engl.* 19, 779–807. doi: 10.1002/anie.198007791

Segall, M. D., Lindan, P. J. D., Probert, M. J., Pickard, C. J., Hasnip, P. J., Clark, S. J., et al. (2002). First-principles simulation-ideas, illustrations and the CASTEP code. *J. Phys. Cond. Matt.* 14, 2717–2744. doi: 10.1088/0953-8984/14/11/301

Ubaldini, S., Veglio, F., Toro, L., and Abbruzzese, C. (2000). Technical note combined bio-hydrometallurgical process for gold recovery from refractory stibnite. *Miner. Eng.* 13, 1641–1646. doi: 10.1016/S0892-6875(00)00148-5

Vanderbilt, D. (1990). Soft self-consistent pseudopotentials in a generalized eigenvalue formalism. *Phys. Rev. B* 41, 7892–7895. doi: 10.1103/physrevb.41.7892

Wang, C., Xia, J., Liu, H., Zhou, Y., and Nie, Z. (2022). Enhancement mechanism of stibnite dissolution mediated by *Acidithiobacillus ferrooxidans* under extremely acidic condition. *Int. J. Mol. Sci.* 23:3580. doi: 10.3390/ijms23073580

Wang, Z., Xie, X., Xiao, S., and Liu, J. (2010). Adsorption behavior of glucose on pyrite surface investigated by TG, FTIR and XRD analyses. *Hydrometallurgy* 102, 87–90. doi: 10.1016/j.hydromet.2010.01.004

Wang, L., Ye, L., and Jing, C. (2020). Genetic identification of Antimonate respiratory reductase in Shewanella sp. ANA-3. *Environ. Sci. Technol.* 54, 14107–14113. doi: 10.1021/acs.est.0c03875

Wilson, N. J., Craw, D., and Hunter, K. (2004). Antimony distribution and environmental mobility at an historic antimony smelter site, New Zealand. *Environ. Pollut.* 129, 257–266. doi: 10.1016/j.envpol.2003.10.014

Yan, L., Chan, T., and Jing, C. (2020). Mechanistic study for stibnite oxidative dissolution and sequestration on pyrite. *Environ. Pollut.* 262:114309. doi: 10.1016/j.envpol.2020.114309

Yang, H., and He, M. (2015). Speciation of antimony in soils and sediments by liquid chromatography–hydride generation–atomic fluorescence spectrometry. *Anal. Lett.* 48, 1941–1953. doi: 10.1080/00032719.2015.1004077

Yang, Y., Liu, W., Bhargava, S. K., Zeng, W., and Chen, M. (2016). A XANES and XRD study of chalcopyrite bioleaching with pyrite. *Miner. Eng.* 89, 157–162. doi: 10.1016/j.mineng.2016.01.019

Ye, L., Meng, X., and Jing, C. (2020). Influence of sulfur on the mobility of arsenic and antimony during oxic-anoxic cycles: differences and competition. *Geochim. Cosmochim. Acta* 288, 51–67. doi: 10.1016/j.gca.2020.08.007

Zeng, W., Peng, Y., Nan, M., and Shen, L. (2020). Electrochemical studies on dissolution and passivation behavior of low temperature bioleaching of chalcopyrite by *Acidithiobacillus ferrivorans* YL15. *Miner. Eng.* 155:106416. doi: 10.1016/j.mineng.2020.106416

Zhang, Y., Wang, C., Ma, B., Jie, X., and Xing, P. (2019). Extracting antimony from high arsenic and gold-containing stibnite ore using slurry electrolysis. *Hydrometallurgy* 186, 284–291. doi: 10.1016/j.hydromet.2019.04.026

Zhao, C., Yang, B., Wang, X., Zhao, H., Gan, M., and Qiu, G. (2020). Catalytic effect of visible light and Cd^{2+} on chalcopyrite bioleaching. *Trans. Nonferr. Metal. Soc. China* 30, 1078–1090. doi: 10.1016/s1003-6326(20)65279-7

Zheng, X., Cao, S., Nie, Z., Chen, J., and Ling, W. (2020). Impact of mechanical activation on bioleaching of pyrite: a DFT study. *Miner. Eng.* 148:106209. doi: 10.1016/j.mineng.2020.106209

Zheng, X., Liu, L., Nie, Z., Yang, Y., Chen, J., Yang, H., et al. (2019). The differential adsorption mechanism of hexahydrated iron and hydroxyl irons on a pyrite (10 0) surface: a DFT study and XPS characterization. *Miner. Eng.* 138, 215–225. doi: 10.1016/j.mineng.2019.05.006

Zheng, X., Nie, Z., Jiang, Q., Yao, X., Chen, J., Liu, H., et al. (2021). The mechanism by which FeS_2 promotes the bioleaching of $CuFeS_2$: an electrochemical and DFT study. *Miner. Eng.* 173:107233. doi: 10.1016/j.mineng.2021.107233

Zheng, X., Pan, X., Nie, Z., Yang, Y., Liu, L., Yang, H., et al. (2018). Combined DFT and XPS investigation of cysteine adsorption on the pyrite (1 0 0) surface. *Fortschr. Mineral.* 8:366. doi: 10.3390/min8090366